Surface Hydroxyl Identity and Reactivity in Akaganéite

2 AUTHORS, INCLUDING:

Jean-Françoi Boily
Umeå University
87 PUBLICATIONS   1,650 CITATIONS

Surface Hydroxyl Identity and Reactivity in Akaganéite

Xiaowei Song* and Jean-François Boily

Department of Chemistry, Umeå University, SE-901 87, Sweden

S *Supporting Information*

ABSTRACT: Hydroxyl groups on surfaces of well-defined akaganéite (β-FeOOH) particles were identified by Fourier transform infrared spectroscopy. These efforts, assisted by molecular dynamics simulations, enabled the extraction of spectral signatures for these groups of the dominant (100), (001), and (010) crystallographic planes. Band assignments were supported by spectral variations induced by proton and chloride adsorption as well as temperature-programmed desorption. Molecular dynamics simulations were used to determine patterns and free energies of formation of hydrogen bonds. Surface Fe—O distances as well as hydrogen-bond numbers were also used to predict proton affinities. All spectral component concentrations display highly comparable responses to proton loadings with those of other FeOOH minerals previously studied with our coupled experimental—theoretical approach. These similarities underpin common thermodynamic stabilities for hydroxyls of a given Fe nuclearity on different planes of different minerals.
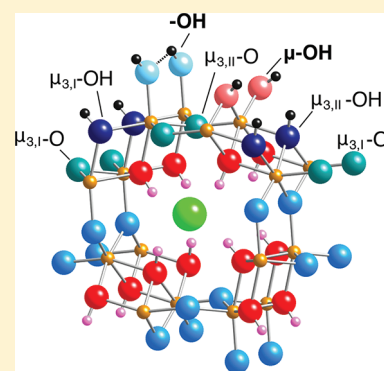
INTRODUCTION

Akaganéite (β-FeOOH), a chloride-bearing ferric oxyhydroxide, has attracted attention in a variety of areas including tunnel-structured nanomaterial development[1−3] and weathering steel corrosion[4,5] as well as sorption science and technology[6−8] and geochemistry.[9−13] This mineral adopts a hollandite-type structure[14] with chloride-bearing channels formed by 2 × 2 chains of edge-sharing iron octahedra (Figure 1). Its bulk properties have been studied by synchrotron X-ray and neutron powder diffraction,[5,15] Mössbauer spectroscopy,[5,16] nuclear magnetic resonance,[17] and Raman[18] and Fourier transform infrared (FTIR)[19,20] spectroscopy. Although its occurrences are generally limited to chloride-bearing environments,[21] akaganéite is involved in contamination scavenging through its abilitiy at regulating anionic and cationic concentrations in natural waters.[6−8] It is a notably strong sorbent material for metal ions and oxyanions (e.g., Cd^{2+}, Zn^{2+}, UO_2^{2+} AsO_4^{3-}, $HCrO_4^{-}$)[6,8−11] given by its large specific surface area as well as high surface site reactivity.

Reactions occurring on the surfaces of this material typically involve hydroxyl groups that are singly ($-OH^{0.5-}$; $\equiv Fe-OH^{0.5-}$), doubly ($\mu-OH^0$; $\equiv Fe_2-OH^0$), and triply ($\mu_3-OH^{0.5+}$; $\equiv Fe_3-OH^{0.5+}$) coordinated to underlying iron atoms. Differences in metal coordination number can strongly affect the ability of these groups in coordinating with metal ions and protons, undergoing ligand exchange, or forming hydrogen bonds. Experimental determination of the identity and distribution of these sites on akaganéite surfaces is therefore central for understanding sorption processes on this important material. Fortunately, hydroxyl groups of FeOOH surfaces can effectively be probed by Fourier transform infrared (FTIR) spectroscopy.[22−24] These groups are typically manifested on the high-energy portion of the O—H stretching region. Spectral variations of this region, induced by changes in surface composition, can help identify distinct

hydroxyl groups as well as possible hydrogen-bonding patterns. This approach has notably been used to probe hydroxyl groups of α- and γ-FeOOH[24,25] surfaces. Similar studies are, however, lacking for akaganéite.

In this study, FTIR spectroscopy is used to probe hydroxyl groups of synthetic akaganéite particles with a well-defined morphology (Figure 1). These particles are ideally terminated by the isostructural (001) and (100) planes[21] both exposing a mixture of −OH, μ-OH, and μ_3-OH sites. The terminal (010) plane exposes, on the other hand, a mixture of μ-OH, μ-O, and geminal η-$(OH_2)_2$ groups with the latter referring to pairs of H_2O chemisorbed to the same Fe atom (Figure 1). These particles, prepared by hydrolysis of $FeCl_3$, are usually of lower specific surface area than those produced in ammonium carbonate media.[26] They are, however, deemed to be more representative of environmental particles, such as those produced in hydrothermal fluids or by chloride-acclimated microorganisms.[13] They are, moreover, free of ammonium and carbonate traces, which may not only dampen but also distort surface OH spectroscopic signatures of pristine akaganéite surfaces.

Experiments carried out for this work were designed to induce systematic changes in the spectroscopic signatures of our akaganéite particles. These changes were made by variations in proton loadings, chloride loadings, and temperature. Chemometric methods are used to extract spectral components of distinct sets of surface hydroxyls. By combining these results with new sets of molecular dynamics (MD) simulations of the dominant akaganéite surfaces, with estimations of proton affinity constants, and with comparisons with our earlier work on other FeOOH polymorphs,[24,25] we propose a conceptual model for understanding the surface
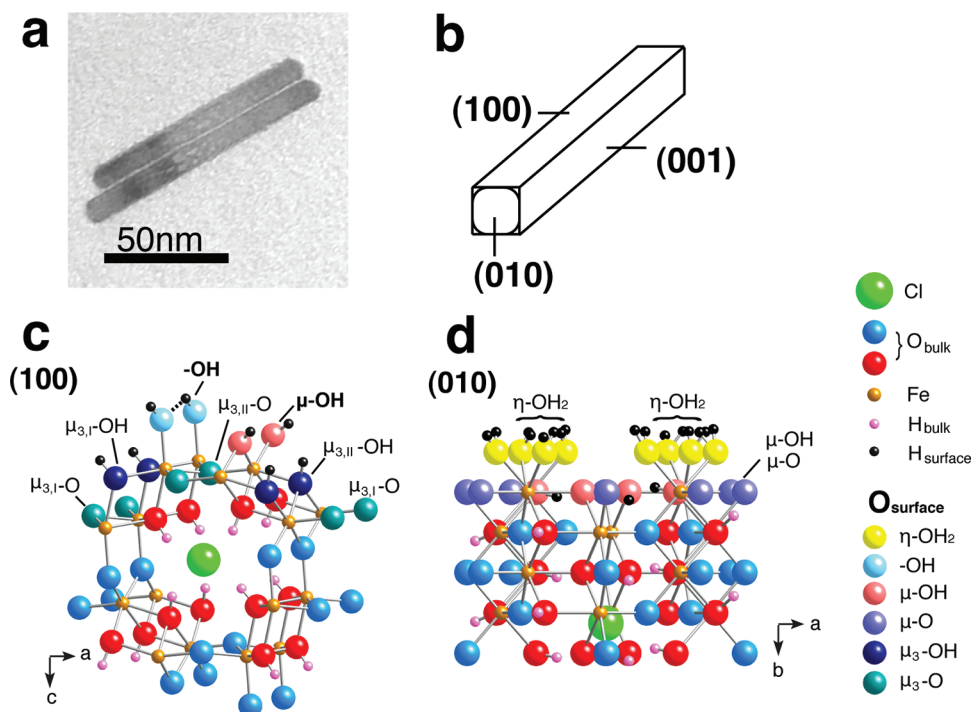
Figure 1. (a) TEM and (b) particle morphology of synthetic akaganéite. Samples were prepared in a CO_2-free atmosphere. Sample purity was confirmed by X-ray diffraction and FTIR spectroscopy. Surface and bulk structures of akaganéite are shown in c and d. Different hydroxyl groups on (c) (100) and (d) (010) surfaces are exposed.

reactivity of this important class of FeOOH minerals in chloride-bearing media.

■ MATERIALS AND METHODS

Materials. Synthetic akaganéite was prepared at 298 K by hydrolysis of a 1 M $FeCl_3$ solution neutralized to a OH/Fe ratio of 0.75.[21] Reactions were carried out in a polyethylene bottle by dropwise addition of 75 mL of a 1 M NaOH solution to a 100 mL $FeCl_3$ solution under continued vigorous stirring and flushing with N_2 (g) (99.996% purity). After a 50 h period of nuclei formation, a 20 mL 10 M NaOH solution was added dropwise under the same conditions, and the resulting suspension was sealed and transferred to an oven at 343 K for 8 days. The precipitates were then washed at room temperature with doubly distilled deionized water (18.2 $M\Omega \cdot cm$), which was first degassed by boiling and then was purged by N_2 (g) overnight. Repeated cycles of centrifugation (5000 rpm, for 60 min) and decantation were carried out until the suspensions could no longer be centrifuged. The suspensions were thereafter dialyzed in porous membranes (Spectra/Por, Spectrum Laboratories) for a period of 3 weeks at 298 K until the conductivity of water retained a value larger than 200 $K\Omega \cdot cm$ for over 7 consecutive days. The residual salt concentration (0.35 mM NaCl, inferred by conductivity measurements) results from the equilibration of akaganéite with the aqueous solution.[27] This result contrasts markedly with our dialysis results of other FeOOH polymorphs, typically leading to supernatant solutions with conductivity values in the range of doubly distilled deionized water, and will be discussed in greater detail in a forthcoming paper focused on akaganéite/water interfaces. The resulting suspension was stored in sealed polyethylene bottles stored in a N_2(g) filled desiccator to minimize any contact with atmospheric CO_2.

A portion of this suspension was dried in a glass vessel a 343 K for 7 days under an atmosphere of N_2(g). It was then ground to a powder in an agate mortar.

The ground material was used for physical and chemical characterization. The akaganéite structure was investigated by power X-ray diffraction (XRD) with a Bruker d8 Advance instrument working in $\theta-\theta$ mode and with Cu Kα radiation (see Figure S1 of the Supporting Information). FTIR measurements (see Figure S1 of the Supporting Information) were also carried out on dry particles with the setup described in the following section. Specific surface area and microporosity were determined from a 90 point N_2(g) adsorption/desorption isotherm (TriStar, Micrometrics). These measurements were carried out on samples previously dried in situ at 110 °C for 16 h under a stream of N_2(g). Finally, X-ray photoelectron spectroscopy (XPS) was carried out using a Kratos Axis Ultra electron spectrometer equipped with a delay line detector. More details on the instrument setup can be found in the recent XPS study of Shimizu et al.[28] Finally, transmission electron microscopy imaging was carried out in an akaganétite—water mixture using a JEM-1230 (JEOL) instrument.

ATR-FTIR Spectroscopy. FTIR measurements of dry akaganéite particles were used to monitor variations in O—H stretching vibrations of OH groups induced by reactions with various proton and chloride loadings. These samples were prepared from aqueous suspensions of akaganéite (44.29 g/L, initial pH 5.0) reacted with different concentrations of standardized solutions of HCl, NaOH, or NaCl (see Tables S3 and S5 of theSupporting Information). These suspensions were equilibrated for 24 h and were exposed to N_2(g) for another 0.5 h prior to centrifugation. The centrifuged wet pastes were then transferred onto an attenuated total reflectance (ATR) cell (Golden Gate, single-bounce diamond) and were dried to a thin film under the
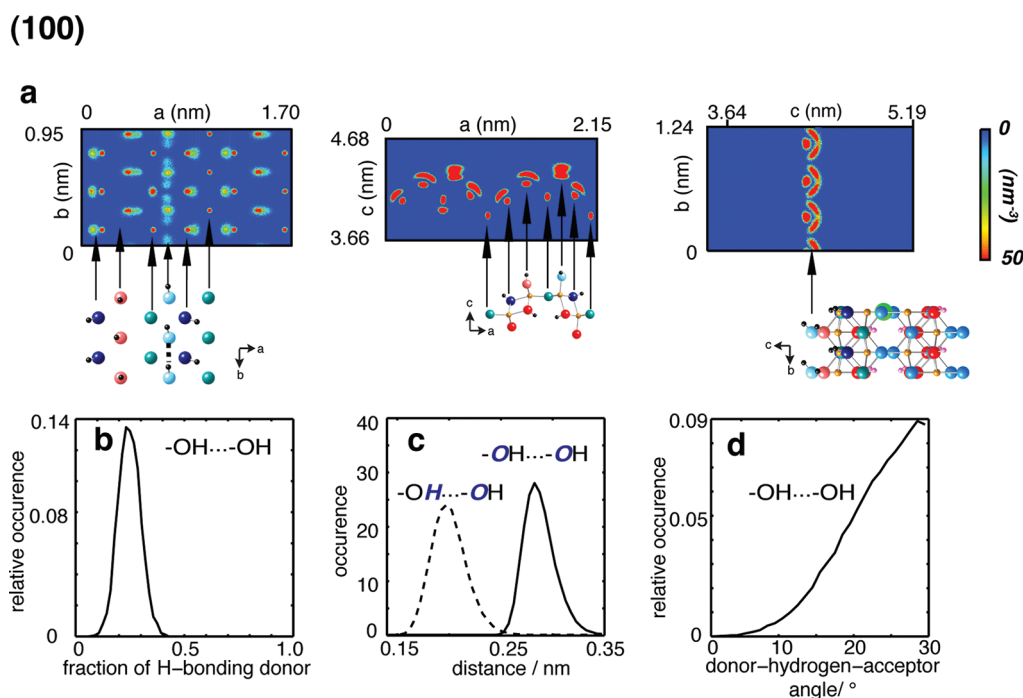
(100)

Figure 2. MD density maps of surface OH sites on (100) plane of akaganéite (a) and hydrogen-bond analyses obtained from MD simulations (b–d). About one-fourth (23.2 ± 0.1%) of the −OH groups donate hydrogen bonds. H-bond donor−acceptor (oxygen−oxygen) distances (c) are shown as solid lines while their corresponding hydrogen-acceptor (hydrogen−oxygen) distances are plotted as dashed lines. Bond angles (d) point to hydrogen bonds uncharacteristic of waterlike bonds. The legend for atoms is shown in the caption of Figure 1.

$N_2(g)$ atmosphere of the analysis chamber of the spectrometer. This procedure increases proton/hydroxyl and chloride loadings beyond levels expected from aqueous suspensions. However, as precipitation (HCl, NaCl) and volatilization (HCl) reactions are also likely to occur, the reported values are not actual surface densities.

FTIR spectra were collected with a Bruker Vertex 70/V FTIR spectrometer using a DLaTGS detector in a room kept at 298 K. Spectra were taken in the $600-4500$ cm^{-1} range at a resolution of 2.5 cm^{-1} at a forward/reverse scanning rate of 10 Hz and were the result of 1000 coadded scans. The Blackman−Harris three-term apodization function was used to correct phase resolution. Spectra were collected every 0.5 h during the water evaporation procedure until O−H stretching and bending modes of free water disappeared. This ensured that the spectra chosen for the chemometric analyses arise from samples equilibrated with $N_2(g)$.

TPD-FTIR Spectroscopy. Temperature-programmed desorption (TPD) was used to expose surface functional groups of akaganéite to controlled temperature gradients. Dry akaganéite powder was heated at a rate of 10 K/min from 318 to 673 K under an operating pressure below 2.5 mTorr, which is the detection limit of the pressure sensor (MKS, Baratron). The setup consists of a reaction chamber equipped with KBr IR windows connected to a turbo vacuum pumping station (Pfeiffer Vacuum, HiCube 80 Eco). The powder was pressed onto a fine tungsten mesh (Unique Wire Weaving, 0.002″ mesh diameter) squeezed into a copper-heating shaft and in direct contact with a K-type thermocouple. A background spectrum was collected in the absence of akaganéite under identical conditions. All spectra were collected using the aforementioned acquisition protocol except that each spectrum was an average of 25 scans at a resolution of 4 cm^{-1}. This was necessary to collect a sufficient number of spectra during TPD.

Chemometrics Analyses. All spectra were analyzed by chemometric methods[29] under the computational environment of Matlab 7.0 (The Mathworks, Inc.). All reported absorbances are therefore arbitrary units as they were offset to zero absorbance value at 4450 cm^{-1}, where absorbances are negligible. All spectra were baseline-corrected and were normalized for area in the bulk OH stretching region. Singular value decomposition (SVD)[30] and factor indicator function (IND)[31] calculations were used to determine the dimensionality of the data set. A description of these methods in the context of FTIR studies of FeOOH minerals can be found in Boily and Felmy.[24] These analyses were used to reconstruct noise/error-reduced spectra using chemically relevant (eigen) vectors. A multivariate curve resolution (MCR) analysis of these results was then carried out with MCR-ALS.[32] This analysis extracted linearly independent spectral components (ε) as well as their corresponding relative fractions (C). These results can be used to reproduce the data using the Beer−Lambert law (εC). The SIMPLISMA (simple-to-use interactive self-modeling mixture analysis) algorithm[33] was also used on the same data set as a comparison and validation. In addition, two-dimensional correlation spectroscopy (2D-CS)[34] was used to identify independent sets of bands arising from distinct species. These calculations were generated and mapped using a code that handles data sets of unevenly spaced concentrations.[35]

Molecular Dynamics. A $4 \times 14 \times 4$ akaganéite (β-FeOOH) supercell containing 1792 FeOOH units was generated using the crystal structure of Post et al.[15] Chloride ions were emplaced in the channels of akaganéite to achieve a chloride-rich solid with an initial Fe:Cl ratio of 8:1. This was effectively carried out by sequentially concatenating $4 \times 1 \times 4$ supercells with two distinct distributions of chloride ions shown in Figure S2 of the

Supporting Information. Charge compensation was achieved by protonating O2 and O4 sites in the pattern shown in the same figure. Protonation of these groups was deemed more likely in recent density functional theory calculations[36] as well as by Ståhl et al.[5] than the initially proposed (O1)H···H···Cl linkages of Post et al.[15] As the simulations were carried out using the fractional atomic charges of the CLAYFF[37] force field, two O2 or O4 were protonated for each chloride ion instead of one. In this procedure, we substituted two O2/O4 (-1.05×2) for one Cl (-1.00) and two O2H/O4H (-0.525×2). The resulting charge imbalance of -11.2 for 224 chloride original insertions was thereafter counterbalanced by resubstitution of 48 equally spaced hydroxyls for O2/O4 and removal of 14 equally spaced chloride ions. This procedure ensured a neutrally charged $Fe_{1792}O_{1392}(OH)_{2192}Cl_{210}$ supercell with original crystallographically determined dimensions of 4.235 nm × 4.244 nm × 4.206 nm.

This cell was simulated by classical MD with the CLAYFF[37] force field. All parameter values and equations are reported in Table S1 of the Supporting Information (SI). The parameter for Fe^{3+} was, however, taken from Kerisit[38] as it provides more accurate predictions of bulk and surface FeOOH structures than the original CLAYFF parameter. The cells were repeated infinitely in all three dimensions by periodic boundary condition. An NPT (constant number of particles, constant pressure, and constant temperature) ensemble and a time step of 0.5 fs were used to integrate the equations of motions with the Verlet algorithm.[39] The temperature of the whole system (300 K) was coupled to the Nosé-Hoover velocity-rescale thermostat at a 0.1 ps relaxation time. Pressure (750.06 Torr) was coupled using an anisotropic scaling of the simulation box using the Parrinello-Rahman method.[40,41] The LINCS algorithm[42] was used to treat O-H bonds of all hydroxyls. A 0.8 nm cutoff was used for van der Waals interactions, and the particle mesh Ewald method[43,44] was used to treat long-range electrostatics. All calculations were carried out with Gromacs (v.4.5.3).[45]

Simulation cells were first energy-minimized (double precision) using a steepest descent algorithm in typically less than 10^4 steps and were equilibrated (single precision) by classical MD for 10^7 steps at 0.5 fs interval for a total of 5 ns. Additional 5 ns simulations were then generated for production runs to monitor atomic positions and energies. The cell relaxed with average dimensions of -0.47% (a), 1.30% (b), and -0.57% (c) of the crystallographic values. This cell corresponds to a specific gravity of 3.74 g/cm^{3}, consistent with an experimental value[5] of 3.73 g/cm^{3}, which we calculated from the lattice dimension and the $FeO_{0.833}(OH)_{1.167}Cl_{0.167}$ composition of comparable akaganéite samples studied by Ståhl et al.[5] Full results of our bulk structure calculations will be reported in a forthcoming communication.

Our relaxed cell was then cut along the (100) and (010) planes leaving 0.4 nm between each oriented slabs. The (001) plane was not simulated as it is isostructural to (100). OH groups and H atoms were, respectively, added to bare surface Fe atoms and undercoordinated O atoms of the (100) plane to ensure charge neutrality. Each of the two (100) planes of the simulation displayed 56 -OH (3.09 sites/nm[2]), 56 μ-OH (3.09 sites/nm[2]), 112 μ_3-OH (6.18 sites/nm[2]), 42 + 56 μ_3-O (2.32 + 3.09 sites/nm[2]) surface sites, and 14 μ_3-OH (0.77 sites/nm[2]) groups pointing toward tunnel chloride ions (Figures 1 and 2). NPT simulations were then carried out for 5 ns to equilibrate the system followed by another 5 ns production run.
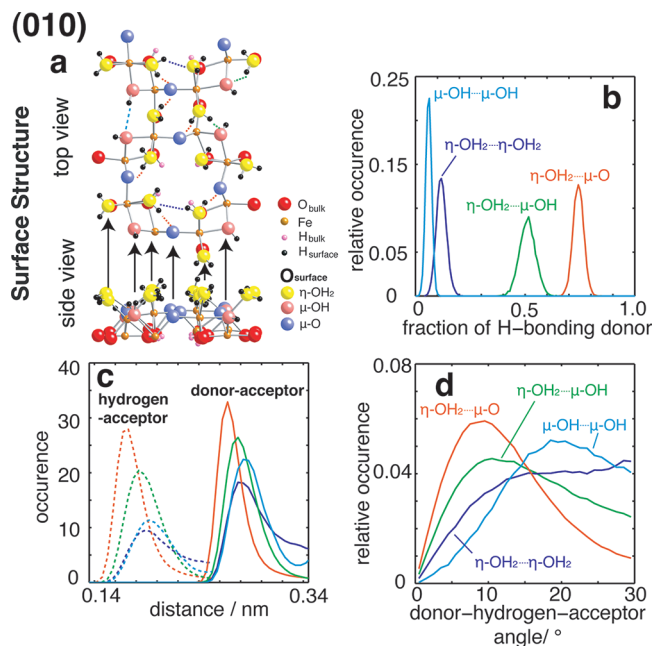

Figure 3. Molecular structure of (010) plane of akaganéite (a) and hydrogen-bond analyses obtained from MD simulations (b-d). The strongest hydrogen bonds occur between η-OH$_2$ and μ-O sites (orange) as well as η-OH$_2$ with μ-OH sites (green) (Table 3). Weaker hydrogen bonds form between μ-OH (light blue) and η-OH$_2$ (dark blue) groups. H-bond donor-acceptor (oxygen-oxygen) distances (c) are shown in solid lines, and their corresponding hydrogen-acceptor (hydrogen-oxygen) distances are plotted as dashed lines.

Each cut (010) surface exposed 128 μ-OH (7.06 sites/nm[2]), 128 μ-O (7.06 sites/nm[2]), and 64 bare Fe (3.53 sites/nm[2]) (Figures 1 and 3). Bare Fe atoms were first reacted with excess flexible Single-Point-Charge model (SPC)[46,47] waters both in the gas ($\ll 1$ g/cm^{3}) and condensed (1 g/cm^{3}) phases. The SETTLE algorithm[48] was, in this case, used to treat the geometry of water in conjunction with LINCS[42] for the O-H bonds. In both cases, each surface Fe stabilized two water molecules henceforth referred to as geminal sites (η-OH$_2$) as these Fe atoms are coordinated to four underlying bulk oxygen atoms. All excess waters were removed from the cell equilibrated in gaseous water leaving exactly two water molecules per bare surface (010) Fe. Simulations were then pursued for a 5 ns equilibration period followed by an additional 5 ns production run.

Surface properties, including hydrogen-bonding distances, angles, and population distributions as well as density maps, were calculated from the trajectories of 5 ns production runs. Equilibrium constants for hydrogen-bonding formation were determined by the hydrogen-bonding population distributions as[49]

$$k_{eq} = \frac{N_{max} - N_{isolate}}{N_{isolate}} \tag{1}$$

where N_{max} is the maximum number of hydrogen bonds for a given surface group and $N_{isolate}$ is the number of isolate (not hydrogen-bonded) groups taken as the median of the population distribution.

■ RESULTS AND DISCUSSIONS

Sample Characterization. X-ray powder diffraction measurements confirmed akaganéite as the only crystallographic phase

17039

dx.doi.org/10.1021/jp204550k |J. Phys. Chem. C 2011, 115, 17036–17045

Table 1. Predicted Proton Affinity Constants of OH Groups of the (100) Surface[a]

			(100) face			
type of group	site density (sites/nm^2)	crystallographic Fe−O length (Å)	proton affinity[b] (log K_{H1}, log K_{H2})	MD Fe−O length (Å)		proton affinity[c] (log K_{H1}, log K_{H2})
−O	3.09	1.946	19.6, 7.7 ($\cdots$−OH$\cdots$)	1.96	20.0,	8.2 ($\cdots$−OH$\cdots$)[d]
						12.1 (−OH$\cdots$)
						4.2 ($\cdots$−OH)
						8.2 (−OH)
μ-O	3.09	1.985	9.9, −1.94	2.00, 2.00	10.8, −1.1	
$\mu_{3,I}$-O(H)	3.09	2.054, 2.054, 2.104	9.72	2.10, 2.10, 2.10	11.74	
$\mu_{3,II}$-O(H)	3.09	2.129, 2.129, 2.070	12.27			
$\mu_{3,I}$-O	3.09	1.945, 1.945, 1.977	0.32	1.98, 1.98, 1.98	2.59	
$\mu_{3,II}$-O	3.09	1.945, 1.945, 1.977	0.32			

[a] Predicted proton affinities of OH groups on the isostructural (100) face are listed in SI, Table S2. [b] Predicted from crystallographic distances. [c] Predicted by MD simulations. As 23.2 ± 0.1% of −OH groups form hydrogen bonds, log K_{H2} values are reported for different hydrogen-bonding patterns. [d] Hydrogen-bonding type listed in the brackets. $\cdots$−OH$\cdots$ H-bond donor and acceptor; −OH$\cdots$ H-bond acceptor; $\cdots$−OH H-bond acceptor; −OH isolate −OH without H-bonding.

present in the samples (Figure S1 of the Supporting Information). FTIR spectra also confirm these findings through characteristic O−H stretching (3490, 3410 cm^{-1}) and bending (800, 685, 615 cm^{-1}) modes only (Figure S1 of the Supporting Information).[19,20] XPS results retrieved a Fe:Cl ratio of 6, consistent with the experimental composition of Ståhl et al.,[5] and confirmed the absence of contaminants other than the usual aliphatic carbon associated to these in-vacuo measurements.

Particles are acicular in shape (7−10 nm × 80−110 nm) (Figure 1) and, on the basis of crystallographic considerations, ~95% of their surfaces are equally represented by the isostructural (100) and (001) planes leaving only ~5% of the remaining area by the terminal (010) plane. These particles are associated with a N$_2$(g) Brunauer−Emmett−Teller (BET) specific surface area of 111.2 m^2/g (microporosity of 4% and Barret−Joyner−Halenda pore diameter of 7.4 nm). This value falls on the lower end (110−160 m^2/g) of those that can be calculated from our particle dimensions and a specific gravity[5] of 3.73 g/cm^3. Therefore, although surface microporosity may account for some imperfections, the close correspondence of our BET values to those calculated with particle size supports our efforts in comparing theoretical structures with the experimental data. The theoretical structures will first be discussed to provide a description of ideal akaganéite surfaces. These results will then be used to support interpretation of the experimental data in the latter part of this paper.

Surface Structure and Site Distribution. MD simulations of the relaxed (100) plane, and by analogy the (001) plane, retrieve Fe−O distances within 0.05 Å of crystallographic values (Table 1, Figure 2). This relaxed and neutrally charged surface exhibits an array of isolate μ-OH^0, μ_3-O$^{0.5-}$, μ_3-OH$^{0.5+}$ groups as well as rows of −OH$^{0.5-}$ groups along the b-axis. These latter groups form hydrogen bonds with neighboring −OH$^{0.5-}$ groups during 23.2 ± 0.1% of the simulation. The median donor−acceptor bond length (0.283 nm) is typical of hydrogen bonding but the angle, peaking at 28.5°, is considerably larger (e.g., 12°) than typical hydrogen bonds. Consistent with these results, the bonds are relatively weak in energy (ΔG = 0.36 kJ/mol) compared to SPC water (ΔG = −4.55 kJ/mol).[49] Their formation should nonetheless affect spectroscopic signatures of these groups as will be suggested in the following sections.

Hydrogen bonding is also expected to impact protonation reactions estimated here as p$K_{H1,H2}$ values using crystallographic and MD Fe−O distances (Table 1) with the multisite complexation (MUSIC) model.[50,51] Values for the (001) plane are reported in Table S2 of the Supporting Information. This approach suggests that isolate ([−OH −**OH** −OH]) sites should possess identical proton affinities to those forming continuous chains of hydrogen bonds ([−OH$\cdots$−**OH**$\cdots$−OH$\cdots$]). Those forming discontinuous chains, as in our case, should, however, exhibit different affinities for protons. Indeed, groups that only donate but do not receive a hydrogen bond ([−OH −**OH**$\cdots$−OH]), namely, a quarter of the sites in our simulations, have affinities that are 4 orders of magnitude larger than isolate groups represented by half of the sites. Conversely, the remaining sites, which are acceptors of the type [−OH$\cdots$−**OH** −OH], have the lowest proton affinity (pK_{H2} = 4.2). Obviously, variations in hydrogen-bonding patterns brought by (de)protonation will impact distributions of these affinity constants. Proton affinities for μ-O$^{1.0-}$ and μ_3-O$^{0.5-}$ are, in contrast, not affected by hydrogen bonding. These sites are represented by the μ-OH^0 and μ_3-OH$^{0.5+}$ species under circumneutral conditions (Figure S3 of the Supporting Information). Overall, this speciation scheme is reminiscent of the (110) plane of goethite[50] with the exception that about three sites/nm^2 μ_3-OH$^{0.5+}$ of goethite are present as μ_3-O$^{0.5-}$ in akaganéite. A thermodynamic surface complexation model using our calculated values (Figure S3 of the Supporting Information) consequently predicts a point of zero charge of 8.2 for the (100)/(001) planes of akaganéite compared to 9.4 for the (110) of goethite.

The terminal (010) plane of akaganéite exposes μ-OH^0, μ-O$^{1.0-}$, and bare Fe sites stabilized by geminal waters which each possess a formal charge of 0.5+ such that η-(H$_2$O)$_2^{1.0+}$. MD simulations of this relaxed plane retrieve Fe−O(H) distances within 0.06 Å of crystallographic values (not counting water) (Figure 3, Table 2). Geminal waters are resilient to desorption once exposed to vacuum during the time scale (5 ns) of the MD simulations. These waters form hydrogen bonds with one another (12% of waters, ΔG = 5.04 kJ/mol) as well as with μ-O$^{1.0-}$ (74% of waters, ΔG = −2.64 kJ/mol). About half (53%) of the μ-OH^0 sites accept hydrogen bonds from geminal waters, while a smaller fraction (6%, ΔG = 6.75 kJ/mol) forms weak angular bonds with one another (Figure 3). This surface, in contrast to its (100) and

Table 2. Predicted Proton Affinity Constants of OH Groups of the (010) Surface

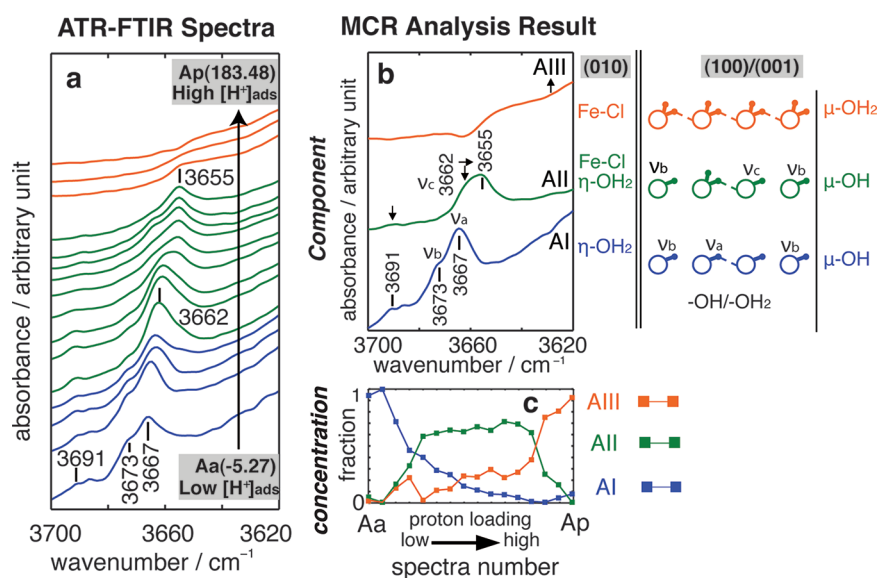| type of group	site density (sites/nm^2)	crystallographic Fe–O length (Å)	proton affinity (log K_{H1}, log K_{H2})	MD Fe–O length (Å)	proton affinity (log K_{H1}, log K_{H2})
			(010) face		
η-OH$_2$	3.53	1.985 (2.129)	$\times^a$	2.10	$\times^a$
	3.53	1.945 (2.054)			
μ-O(H)	3.53	2.104, 2.054	14.78, 2.90	2.04	12.9, 1.06
	3.53	2.129, 2.070	15.68, 3.80		
μ-O	3.53	1.945, 1.977	8.46, −3.40	1.94	7.13, −4.75
	3.53	1.985, 1.946	8.73, −3.15		

^{a} MUSIC model was not applied.

Figure 4. ATR-FTIR spectra of dry synthetic akaganéite in N$_2$ (g). Apparent proton loadings ([H]$_{ads}$: proton/nm^2) in the brackets (a) are derived from [HCl]−[NaOH] values initially present in aqueous suspensions of minerals prior to centrifugation and drying. These values, therefore, do not pertain to the actual amount of protons complexed to mineral surfaces. Variations in band positions and intensities are summarized in Table S3. Spectra (a) are color-coded according to the dominant component (b, c). Arrows (↕) denote intensity changes and (⟷) denote band shifts while black rectangles (▼) denote stable bands. Schematic representation along proton loadings is shown on the right.

(001) counterparts, is therefore rich in hydrogen bonding, which is a characteristic feature of growth planes of FeOOH minerals, such as the (021) plane of goethite.[25,52] Proton affinities of μ-OH^0 are comparable to those of the (100)/(001) plane pointing to a dominance of this species under circumneutral conditions. Those of μ-O$^{1.0−}$ are comparable to those of −OH$^{0.5−}$, given shorter Fe–O distances, and suggest that these groups are responsible for charge uptake under normal conditions as well. Although dissociation constants were not obtained for geminal waters, analogies with −OH groups of the (100)/(001) planes point to a strong buildup of negative charges because of deprotonation under circumneutral to alkaline conditions (Figure S3-c of the Supporting Information).

Overall, the strongest hydrogen bonds on the akaganéite surfaces involve those of η-(H$_2$O)$^{0.5+}$ with μ-O$^{1.0−}$ and μ-OH^0 sites on the (010) plane followed by those of −OH$^{0.5−}$ sites on (100)/(001) planes. This conceptual model will henceforth be used as an interpretive framework to assign vibrational spectra.

Surface Site Identity and Reactivity. Hydroxyl functional groups of the akaganéite surface exhibit characteristic discrete-like stretching vibration bands above 3620 cm$^{−1}$ (Figure 4).

Bands below this value, although resolved in other FeOOH phases,[20,24] could not be identified in akaganéite because of strong overlap with bulk OH stretches[19,20] (3300−3490 cm$^{−1}$). All resolvable surface−OH stretches undergo systematic variations both in position and intensity with proton loading as summarized in Table S3 of the Supporting Information. The 3691 and 3673/3667 cm$^{−1}$ bands dominate the spectra of the most alkaline surfaces (Figure 4a, Aa−Ad). The 3691 cm$^{−1}$ band is persistent to high proton loadings but is subdued by levels exceeding 1.63 protons/nm^2 (spectrum Ah) The 3673/3667 cm$^{−1}$ bands are, in contrast, highly sensitive to proton loadings and shift to 3662 cm$^{−1}$. Loadings exceeding 1.63 protons/nm^2 (Ah), however, consume the 3662 cm$^{−1}$ as well as the broader 3700−3620 cm$^{−1}$ region. This results in a general decrease in the baseline exposing a band centered at 3655 cm$^{−1}$ (Am) that was barely resolvable at lower proton loadings. This band persists to loadings as high as 32.62 protons/nm^2 (Am) but finally subsides under the higher values (63.82 protons/nm^2, An) considered in this study. The three largest proton loadings are characterized by broad red-shifted intensities and a lack of discrete-like stretching vibrations.

Table 3. Equilibrium Constant (eq 1) and Gibbs Free Energy for Hydrogen Bond Formation

H-bond species	k_{eq}	ΔG (KJ/mol)
(010) Face		
η-OH$_2$···η-OH$_2$	0.13	5.04
η-OH$_2$···μ-OH	1.06	−0.16
η-OH$_2$···μ-O	2.88	−2.64
μ-OH···μ-OH	0.07	6.75
(100) Face		
−OH···−OH	0.87	0.36

Table 4. Summary of Band Assignments

wavenumber (cm^{-1})	surface species	crystal plane
3691	η-OH$_2$	(010)
3673	isolate −OH[a]	(100)/(001)
3667	−OH ··· −**OH** −OH	(100)/(001)
3662	−OH$_2$ ··· −**OH** −OH	(100)/(001)
3655	μ-OH	(100)/(001)

[a] Singly coordinated hydroxyls have different band positions under distinct hydrogen-bonding environments. [isolate −OH]: without H-bonding; [−OH ··· −**OH** −OH]: accept H-bond form vicinal −OH; [−OH$_2$ ··· −**OH** −OH]: accept H-bond form vicinal chemisorbed water −OH$_2$.

All spectral features of the protonation series are well captured by MCR (Figure 4b, c). Three pure spectral components reproduce 99.7% of the variance of the data and undergo systematic changes with proton loadings. Similarly, SIMPLISMA extracted three comparable components (Figure S4 of the Supporting Information). MCR component AI dominates alkaline surfaces and consists of bands at 3691 and 3667 cm^{-1}. MCR component AII isolates a broad band centered at 3655 cm^{-1}. This component accounts for most spectral features up to 32.62 protons/nm^2 (Am). Finally, MCR component AIII is associated to an even broader, yet attenuated, band around 3650 cm^{-1} and to broad ranges of intensities below 3630 cm^{-1}. This component is predominant in spectra representative of the three greatest proton loadings (An−Ap). Assignment of these various band sets will now be made on the basis of their relative intensities and responses to proton loadings but also, as will be discussed shortly, to chloride loadings as well as to temperature. A summary of these assignments is reported in Table 4.

Spectral Component AI. The dominant 3667 cm^{-1} band of component AI is predominantly assigned to rows of −OH groups of the (100) and (001) planes. This assignment is in part motivated by previous assignments of similar band sets to rows of −OH groups on the (110) plane of goethite[24] and the (001) plane of lepidocrocite (SI). The latter, in particular, exhibits a highly comparable hydrogen-bonding pattern along −OH rows, generates a strong band at 3667 cm^{-1} (Table S4 and Figures S5 and S6 of the Supporting Information), and responds in the same way to proton loadings with a shift to 3662 cm^{-1}. The absence of asynchronous correlation squares between 3667 and 3662 cm^{-1} in the 2D-CS map of Figure 5 confirms that intensities of both bands vary synchronously. As this 5 cm^{-1} shift should correspond to an increase in O−H distance of only 0.03 pm, given previous accounts[53] pointing to shifts about 175 cm^{-1}/pm, it
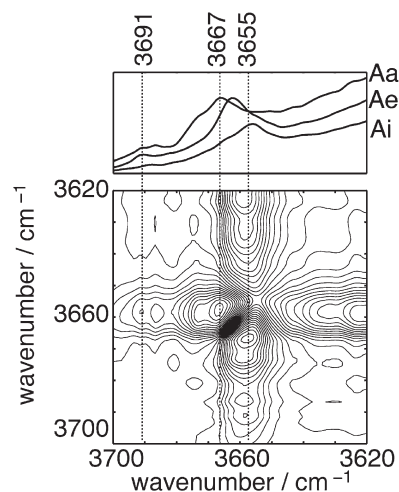
Figure 5. Asynchronous 2D correlation spectrum of Aa to Ap (Figure 4). Representative spectra are also shown.
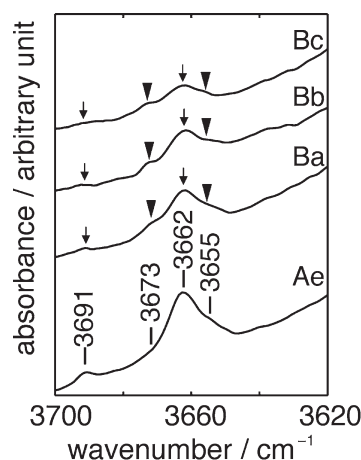
Figure 6. ATR-FTIR spectra of chloride reacted with akaganéite (Ba-Bc). Spectrum of original akaganéite suspension (Ae) is shown as a reference. Arrows (↓) denote intensity loss while black rectangles (▼) denote stable bands.

should most realistically arise from a mild change in the hydrogen-bonding environment. Conversion of −OH$^{0.5-}$ to −OH$_2$$^{0.5+}$ should, in contrast, rather result in a strong shift in the order of several decades in cm^{-1} as suggested in previous work.[25] This proton-induced 5 cm^{-1} shift is consequently proposed to arise from a −OH$^{0.5-}$ group accepting a mildly stronger hydrogen bond from a vicinal −OH$_2$$^{0.5+}$ site, namely, [−OH$_2$···−**OH** −OH] with −**OH** at 3662 cm^{-1} while −**OH** in [−OH··· −**OH** −OH] corresponds to 3667 cm^{-1}.

The 3673 cm^{-1} shoulder of the −OH 3667 cm^{-1} band is another salient attribute of component AI. This shoulder is assigned to isolate −OH groups that neither donate nor receive hydrogen bonds ([−OH −**OH** −OH]). This assignment falls in line with the concept that a higher stretching energy is associated with a shorter bond. Another piece of evidence lies in the expected weaker response such as isolate sites (pK_{H2} = 8.2) to proton loadings compared to those donating a hydrogen bond (pK_{H2} = 12.2) (Table 1) as can be seen in Figure 4. This assignment finds additional support in the chloride-loading data (Figure 6,

Table S5 of the Supporting Information). These data reveal a preferential loss of 3662 cm^{-1} over 3673 cm^{-1}, namely, converting $[-OH_2 \cdots -OH -OH]$ to $[-Cl -OH -OH]$ potentially explaining the intensification of the 3673 cm^{-1} band as well. This preferential consumption can be furthermore explained by a energetically less demanding displacement of the vicinal H_2O rather than $-OH$.

A final, albeit minor, band of component AI occurs at 3691 cm^{-1}. This band, in contrast to 3667 cm^{-1}, is resilient to changes in proton loadings and therefore also occurs in component AII. TPD experiments (Figure 7), moreover, show that it is readily decreased by temperatures as low as 336 K, while all other bands maintain their original intensities and positions. These two properties point to geminal waters of the (010) plane, which is an assignment also finding support in the expectation for weaker intensities arising from a site of overall lower density (i.e., 5% × 7.06 sites/nm^2). The 2D-CS asynchronous map (Figure 5) reveals a clear asynchronous correlation square[34] between 3691 and 3667 cm^{-1} suggesting that these respective regions operate separately. An additional line of evidence to our proposed assignment lies in the response of these bands to chloride loadings (Figure 6).
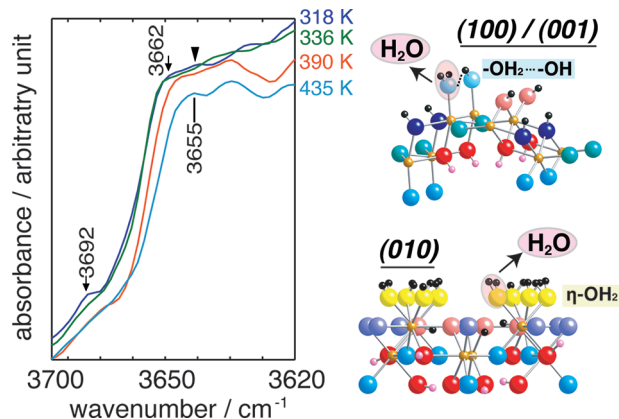
The greater sensitivity of 3691 cm^{-1} (η-OH$_2$) compared to 3673/3667 cm^{-1} ($-OH$) points to a greater ability for η-OH$_2$ to exchange for chloride ions and thereby to form Fe–Cl species. Chloride coordination, moreover, explains the suppression of 3691 cm^{-1} at the greatest HCl loadings (Figure 4). Assignment of 3691 cm^{-1} to η-OH$_2$ sites of the (010) plane of akaganéite consequently provides the best account of all these spectral features.

Spectral Component AII. Component AII is characterized by an intense band centered at 3655 cm^{-1}. This band is also present in component AI but with intensities overshadowed by those of 3673/3667 cm^{-1}, which is a result also confirmed by SIMPLISMA calculations (Figure S4 of the Supporting Information). The 3655 cm^{-1} band is resolved through the protonation series as well as through TPD experiments where thermal desorption of chemisorbed waters led to its detection at temperatures exceeding 390 K (Figure 7). A 2D-CS map of the protonation series (Figure 5) confirms that this band is not correlated to $-OH^{0.5-}$ groups (3667 cm^{-1}). Its behavior with respect to proton loadings is revealing. The weak proton loading dependence of this band, compared to $-OH^{0.5-}$, points to a hydroxyl of greater Fe nuclearity. This is further supported in the weaker response of the 3655 cm^{-1} band to chloride exchange than 3667/3673 cm^{-1} ($-OH^{0.5-}$) as well as in the TPD data showing a resilience to desorption at temperatures as high as 435 K. Interestingly, many of these attributes are highly comparable to μ-OH^0 groups of lepidocrocite (3625 cm^{-1}, cf. Figures S5 and S6 of the Supporting Information) and goethite (3648 cm^{-1}).[24,25] These minerals even display highly comparable fractions of component AII with proton loading (Figure 8). For these reasons, the 3655 cm^{-1} band is assigned to μ-OH^0.

Finally, assignment to μ_3-OH$^{0.5+}$ sites cannot be realized at this point. Expected smaller O–H bond polarizabilities, compared to others of lower iron nuclearities, may however contribute to low spectral intensities. Drawing analogies from the (100) surface of lepidocrocite could, moreover, point to strongly overlapping vibrations with those of the akaganéite bulk.

Spectral Component AIII. The third and last spectral component extracted from the protonation series of akaganéite, AIII, contains characteristic features of heavily protonated surfaces. Similar components were extracted for goethite[24,25] and lepidocrocite (Figures S5 and S6 of the Supporting Information) and exhibit

Figure 7. TPD-FTIR spectra of the dry powder sample of akaganéite. The right-hand side of the figures contains schematic representations of TPD processes on (010) and (001)/(100) surface. The legend for atoms is shown in Figure 1.
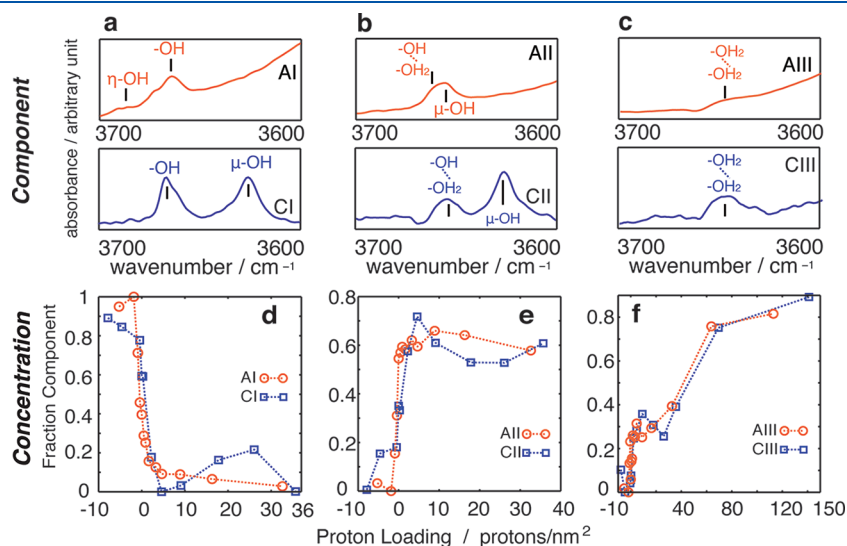
Figure 8. MCR components (a–c) and corresponding concentration profiles (d–f) of akaganéite (orange) and rod lepidocrocite (blue).

broad frequencies shifted to the red in contrast to the tighter discretelike stretches of components AI and AII. These features arise from an extended network of hydrogen bonds between various chemisorbed waters ($-OH_2^{0.5+}$, μ-$OH_2^{1.0+}$) as well as any remaining hydroxyl groups notably including the unresolved μ_3-$OH^{0.5-}$ species. Intensities in the higher stretching energy region are also subdued by iron-bound chloride ion species ($-Cl^{0.5-}$, μ-Cl^0) likely formed under these conditions.

Component Fractions. All MCR components are associated to concentration fractions undergoing systematic variations with proton loadings (Figure 8). As stated earlier, component AI dominates in samples equilibrated under the most alkaline conditions. Its concentration fractions decrease sharply with proton loadings well below 5 protons/nm^2 (Aj). Variations in the collection of bands near 3667 cm^{-1} are responsible for these changes and result from protonation reactions involving $-OH^{0.5-}$ groups. Comparisons of this band set to those of the (100) plane of rod lepidocrocite can be extended to component fractions as shown in Figure 8a. Strong similarities in these loadings point to highly comparable proton affinities for $-OH^{0.5-}$ groups of akaganéite and lepidocrocite. These comparisons also apply to μ-OH^0 sites of akaganéite (AII) and lepidocrocite. An important distinction, however, lies in the smaller frequency of the lepidocrocite band (3625 cm^{-1}), a result possibly arising from differences in Fe$-$O bond strengths as well as from potentially greater iron-proton repulsion associated to the lepidocrocite structure. Therefore, recalling the large sensitivity of O$-$H bond lengths to frequency (175 cm^{-1}/pm), these results show that frequency may not necessarily directly correlate to proton affinity. Finally, component AIII also exhibits nearly overlapping concentration profiles with its lepidocrocite counterpart (Figure 8). This similarity denotes comparable energetic requirements for the formation of extended networks of hydrogen-bonded surface sites on both minerals. Implications of these findings will notably be demonstrated in forthcoming studies on gas-phase sorption reactions involving water and carbon dioxide.

CONCLUSIONS

This work provides spectroscopic tools that can be used to track reactions involving important surface OH groups of different crystallographic planes of akaganéite. We underscored similarities between the (100)/(001) planes of akaganéite and the (001) plane of lepidocrocite. These similarities are most strikingly reflected in overlapping concentration profiles of all spectra components of these two minerals. This relationship underpins common thermodynamic stabilities for hydroxyls of a given coordination number with Fe on different planes of different minerals. As such similarities were also drawn with goethite,[24,25] this observation may potentially be extended to a wider range of FeOOH polymorphs. This notably opens possibilities for resolving surface hydroxyls on related minerals with less well-defined particle morphologies, such as ferrihydrite[54−56] or schwertmannite.[57−59] The impact of such findings on sorption mechanisms, notably those of water vapor physisorption and ultimately condensation, is also the object of ongoing investigations in our laboratory and will be communicated shortly.

ASSOCIATED CONTENT

ⓢ Supporting Information. This material is available free of charge via the Internet at http://pubs.acs.org.

AUTHOR INFORMATION

Corresponding Author
*E-mail: xiaowei.song@chem.umu.se; phone: +46 90 786 5361.

REFERENCES

(1) Dahoumane, S. A.; Djediat, C.; Yepremian, C.; Coute, A.; Fievet, F.; Brayner, R. *Thin Solid Films* **2010**, *518* (19), 5432–5436.
(2) Song, Y.; Bac, B. H.; Lee, Y. B.; Kim, M. H.; Kang, I. M. *Crystengcomm* **2011**, *13* (1), 287–292.
(3) Wei, C. Z.; Nan, Z. D. *Mater. Chem. Phys.* **2011**, *127* (1−2), 220–226.
(4) Reguer, S.; Mirambet, F.; Dooryhee, E.; Hodeau, J. L.; Dillmann, P.; Lagarde, P. *Corros. Sci.* **2009**, *51* (12), 2795–2802.
(5) Ståhl, K.; Nielsen, K.; Jiang, J. Z.; Lebech, B.; Hanson, J. C.; Norby, P.; van Lanschot, J. *Corros. Sci.* **2003**, *45* (11), 2563–2575.
(6) Deliyanni, E. A.; Peleka, E. N.; Matis, K. A. *J. Hazard. Mater.* **2007**, *141* (1), 176–184.
(7) Kolbe, F.; Weiss, H.; Morgenstern, P.; Wennrich, R.; Lorenz, W.; Schurk, K.; Stanjek, H.; Daus, B. *J. Colloid Interface Sci.* **2011**, *357* (2), 460–465.
(8) Yusan, S.; Erenturk, S. A. *Desalination* **2010**, *263* (1−3), 233–239.
(9) Deliyanni, E. A.; Bakoyannakis, D. N.; Zouboulis, A. I.; Matis, K. A. *Chemosphere* **2003**, *50* (1), 155–163.
(10) Deliyanni, E. A.; Matis, K. A. *Sep. Purif. Technol.* **2005**, *45* (2), 96–102.
(11) Lazaridis, N. K.; Bakoyannakis, D. N.; Deliyanni, E. A. *Chemosphere* **2005**, *58* (1), 65–73.
(12) Waychunas, G. A.; Kim, C. S.; Banfield, J. F. *J. Nanopart. Res.* **2005**, *7* (4−5), 409–433.
(13) Xiong, H. X.; Liao, Y. H.; Zhou, L. X. *Environ. Sci. Technol.* **2008**, *42* (23), 8681–8686.
(14) Mackay, A. L. *Mineral. Mag.* **1962**, *33*, 270–280.
(15) Post, J. E.; Heaney, P. J.; Von Dreele, R. B.; Hanson, J. C. *Am. Mineral.* **2003**, *88* (5−6), 782–788.
(16) Garcia, K. E.; Barrero, C. A.; Morales, A. L.; Greneche, J. M. *Rev. Fac. Ing.-Univ. Ant.* **2009**, *49*, 185–191.
(17) Kim, J.; Grey, C. P. *Chem. Mater.* **2010**, *22* (19), 5453–5462.
(18) Remazeilles, C.; Refait, P. *Corros. Sci.* **2007**, *49* (2), 844–857.
(19) Murad, E.; Bishop, J. L. *Am. Mineral.* **2000**, *85* (5−6), 716–721.
(20) Weckler, B.; Lutz, H. D. *Eur. J. Solid State Inorg. Chem.* **1998**, *35* (8−9), 531–544.
(21) Schwertmann, U.; Cornell, R. M., *The Iron Oxides*; Wiley-VCH: Weinheim, Germany, 2003.
(22) Russell, J. D.; Parfitt, R. L.; Fraser, A. R.; Farmer, V. C. *Nature* **1974**, *248* (5445), 220–221.
(23) Lefevre, G. *Adv. Colloid Interface Sci.* **2004**, *107* (2−3), 109–123.
(24) Boily, J. F.; Felmy, A. R. *Geochim. Cosmochim. Acta* **2008**, *72* (14), 3338–3357.
(25) Song, X.; Boily, J. F. *Phys. Chem. Chem. Phys.* **2011**, submitted.
(26) Deliyanni, E. A.; Bakoyannakis, D. N.; Zouboulis, A. I.; Matis, K. A.; Nalbandian, L. *Microporous Mesoporous Mater.* **2001**, *42* (1), 49–57.
(27) Refait, P.; Génin, J. M. R. *Corros. Sci.* **1997**, *39* (3), 539–553.
(28) Shimizu, K.; Shchukarev, A.; Boily, J. F. *J. Phys. Chem. C* **2011**, *115* (14), 6796–6801.
(29) Wold, S. *Chemometr. Intell. Lab.* **1995**, *30* (1), 109–115.
(30) Golub, G. H.; Reinsch, C. *Numer. Math.* **1970**, *14* (5), 403–&.

(31) Malinowski, E. R. *Factor Analysis in Chemistry*, 3rd ed.; John Wiley and Sons: New York, 2002.

(32) Jaumot, J.; Gargallo, R.; de Juan, A.; Tauler, R. *Chemometr. Intell. Lab.* **2005**, *76* (1), 101–110.

(33) Windig, W.; Guilment, J. *Anal. Chem.* **1991**, *63* (14), 1425–1432.

(34) Noda, I.; Ozaki, Y. *Two-Dimensional Correlation Spectroscopy: Applications in Vibrational and Optical Spectroscopy*; John Wiley and sons: Chichester, UK, 2004.

(35) Boily, J. F.; Ilton, E. S. *Surf. Sci.* **2008**, *602* (24), 3637–3646.

(36) Kubicki, J. D. *Personal communication* via email, 2011.

(37) Cygan, R. T.; Liang, J. J.; Kalinichev, A. G. *J. Phys. Chem. B* **2004**, *108* (4), 1255–1266.

(38) Kerisit, S. *Geochim. Cosmochim. Acta* **2011**, *75* (8), 2043–2061.

(39) Hockney, R. W.; Goel, S. P.; Eastwood, J. W. *J. Comput. Phys.* **1974**, *14* (2), 148–158.

(40) Nose, S.; Klein, M. L. *Mol. Phys.* **1983**, *50* (5), 1055–1076.

(41) Parrinello, M.; Rahman, A. *J. Appl. Phys.* **1981**, *52* (12), 7182–7190.

(42) Hess, B.; Bekker, H.; Berendsen, H. J. C.; Fraaije, J. *J. Comput. Chem.* **1997**, *18* (12), 1463–1472.

(43) Darden, T.; York, D.; Pedersen, L. *J. Chem. Phys.* **1993**, *98* (12), 10089–10092.

(44) Essmann, U.; Perera, L.; Berkowitz, M. L.; Darden, T.; Lee, H.; Pedersen, L. G. *J. Chem. Phys.* **1995**, *103* (19), 8577–8593.

(45) van der Spoel, D.; Lindahl, E.; Hess, B.; Groenhof, G.; Mark, A. E.; Berendsen, H. J. C. *J. Comput. Chem.* **2005**, *26* (16), 1701–1718.

(46) Berendsen, H. J. C.; Grigera, J. R.; Straatsma, T. P. *J. Phys. Chem.* **1987**, *91* (24), 6269–6271.

(47) Berendsen, H. J. C.; Postma, J. P. M.; Gunsterenand, W. F.; Hermans, J. *Intermolecular Forces*; D. Riedel Publishing Company: Dordrecht, The Netherlands, 1981; p 331–342.

(48) Miyamoto, S.; Kollman, P. A. *J. Comput. Chem.* **1992**, *13* (8), 952–962.

(49) van der Spoel, D.; van Maaren, P. J.; Larsson, P.; Timneanu, N. *J. Phys. Chem. B* **2006**, *110* (9), 4393–4398.

(50) Venema, P.; Hiemstra, T.; Weidler, P. G.; van Riemsdijk, W. H. *J. Colloid Interface Sci.* **1998**, *198* (2), 282–295.

(51) Hiemstra, T.; Venema, P.; VanRiemsdijk, W. H. *J. Colloid Interface Sci.* **1996**, *184* (2), 680–692.

(52) Russell, B.; Payne, M.; Ciacchi, L. C. *Phys. Rev. B* **2009**, *79*, 16.

(53) Rustad, J. R.; Boily, J. F. *Am. Mineral.* **2010**, *95* (2−3), 414–417.

(54) Arai, Y.; Sparks, D. L. *J. Colloid Interface Sci.* **2001**, *241* (2), 317–326.

(55) Michel, F. M.; Barron, V.; Torrent, J.; Morales, M. P.; Serna, C. J.; Boily, J. F.; Liu, Q. S.; Ambrosini, A.; Cismasu, A. C.; Brown, G. E. *Proc. Natl. Acad. Sci. U.S.A.* **2010**, *107* (7), 2787–2792.

(56) Swedlund, P. J.; Miskelly, G. M.; McQuillan, A. J. *Langmuir* **2010**, *26* (5), 3394–3401.

(57) Knorr, K. H.; Blodau, C. *Appl. Geochem.* **2007**, *22* (9), 2006–2015.

(58) Paikaray, S.; Göttlicher, J.; Peiffer, S. *Chem. Geol.* **2011**, *283* (3−4), 134–142.

(59) Boily, J. F.; Gassman, P. L.; Peretyazhko, T.; Szanyi, J.; Zachara, J. M. *Environ. Sci. Technol.* **2010**, *44* (4), 1185–1190.